

Atomic Scale Investigation of the CuPc-MAPbX₃ Interface and the Effect of Non-Stoichiometric Perovskite Films on Interfacial Structures

Collin Stecker^{1,‡}, Zhenyu Liu^{2,‡}, Jeremy Hieulle^{1,†}, Siming Zhang², Luis K. Ono¹, Guofeng Wang^{2,*}, and Yabing Qi^{1,*}

¹Energy Materials and Surface Sciences Unit (EMSSU), Okinawa Institute of Science and Technology Graduate University (OIST), 1919-1 Tancha, Onna-son, Okinawa 904-0495, Japan.

²Department of Mechanical Engineering and Materials Science, University of Pittsburgh, Pittsburgh, Pennsylvania 15261, United States.

* Corresponding authors: Yabing Qi: Yabing.Qi@OIST.jp; Guofeng Wang: guw8@pitt.edu

ABSTRACT: Metal halide perovskites (MHPs) have become a major topic of research in thin film photovoltaics due to their advantageous optoelectronic properties. These devices typically have the MHP absorber layer sandwiched between two charge selective layers (CSLs). The interfaces between the perovskite layer and these CSLs are potential areas of higher charge recombination. Understanding the nature of these interfaces is key for device improvement. Additionally, non-stoichiometric perovskite films are expected to strongly impact the interfacial properties. In this study, the interface between CH₃NH₃PbI₃ (MAPbI₃) and copper phthalocyanine (CuPc), a hole transport layer (HTL), is studied at the atomic scale. We use scanning tunneling microscopy (STM) combined with density functional theory (DFT) predictions to show that CuPc deposited on MAPbX₃ (X=I,Br) forms a self-assembled layer consistent with the α -polymorph of CuPc. Additionally, STM images show a distinctly different adsorption orientation for CuPc on non-perovskite domains of the thin film samples. These findings highlight the effect of non-stoichiometric films on the relative orientation at the MHP/HTL interface, which may affect interfacial charge transport in a device. Our work provides an atomic scale view of the MHP/CuPc interface and underscores the importance of understanding interfacial structure and the effect that the film stoichiometry can have on interfacial properties.

Keywords: metal halide perovskite, scanning tunneling microscopy, density functional theory, copper phthalocyanine, interfacial properties

Metal halide perovskites (MHPs) have proven to be highly capable photovoltaic materials, with MHP-based solar cells reaching an impressive record power conversion efficiency (PCE) of 25.5%.¹ In these devices, electrons and holes separated in the MHP absorber layer are selectively conducted by an electron transport layer (ETL) and a hole transport layer (HTL), respectively. The interfaces between adjacent layers in MHP-based solar cells are possible areas of increased charge recombination.^{2,3} Interfacial engineering *via* passivation of the perovskite surface has proven a viable strategy for improving device performance.⁴⁻⁶ Additionally, reports have found that non-stoichiometric precursor ratios, achieved during the perovskite film preparation⁷ or *via* post-annealing treatment,⁸ can significantly affect performance. Such non-stoichiometric ratios in the perovskite material are expected to strongly impact the interfacial properties. Using thin interlayers of MAI precursor at the perovskite interface was shown to be a useful method for tuning energy level alignment.⁹ Proper engineering of these interfaces can also result in increased stability.^{4,10} Obtaining a clear understanding of the perovskite/charge selective layer (CSL) interface is crucial for rational interface engineering and further device improvement.

The transition metal phthalocyanines (TMPcs) have been identified as viable HTLs that feature a higher thermal stability than spiro-MeOTAD.¹¹⁻¹⁵ TMPcs have also been utilized as additives in HTLs.¹⁶ Undoped copper phthalocyanine (CuPc) derivatives have been shown

to enable high PCE in MHP-based solar cells.¹⁷ CuPc itself has shown excellent compatibility with low-cost carbon electrodes as well, both as a distinct HTL¹⁸ and as an additive in the carbon electrode,¹⁹ resulting in performance increases. Furthermore, the relatively hydrophobic nature of CuPc enables it to act as a blocking layer from moisture in the environment, delivering impressive stability for unencapsulated devices.^{11,13,18}

Scanning tunneling microscopy (STM) has been shown to be an excellent tool for studying both perovskite surfaces²⁰⁻²⁵ and CuPc molecular and interfacial properties.²⁶⁻²⁸ STM studies of perovskites have determined the surface reconstructions of MAPbI₃, MAPbBr₃ and CsPbBr₃ perovskites,^{20,21,25} and the effect of illumination on the surface structure.²² In addition, STM investigations have shown how surface defects and halide substitution can affect interfacial properties and material stability.^{23,24} Here, utilizing two materials well-suited for STM study, we investigate an MHP/HTL interface by examining sub-monolayer CuPc deposited on MAPbX₃ (X=I, Br) thin films. We reveal that CuPc forms a self-assembled layer on MAPbI₃ and that it behaves differently on non-perovskite domains that may exist in non-stoichiometric perovskite films. This differing behavior has important consequences for interfacial properties and charge transfer in devices.

RESULTS AND DISCUSSION

MAPbI₃ thin films were obtained by co-deposition of PbI₂ and MAI precursor materials onto an Au(111) substrate in a UHV chamber, using methods analogous to those previously reported.²⁰ Following this, CuPc was sublimated onto the MAPbI₃/Au(111) sample, resulting in sub-monolayer coverage (see Methods and Fig. S1 for details).

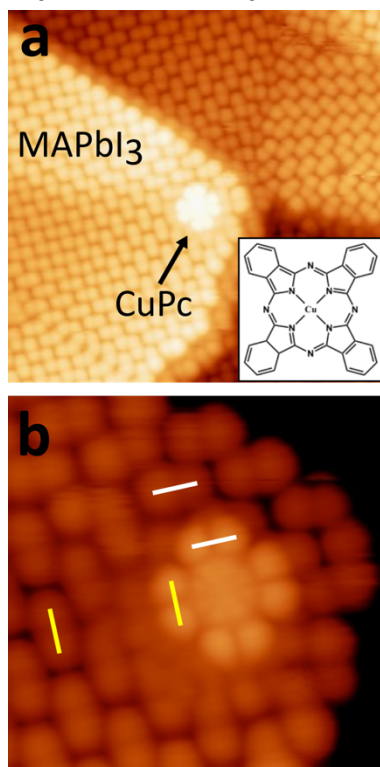


Figure 1. Individual CuPc adsorbed on MAPbI₃ surface. a) Overview STM image of a single, isolated CuPc molecule adsorbed on the (010) MAPbI₃ surface. Inset: Drawing of a CuPc molecule. b) Zoom-in STM image showing the HOMO state of the CuPc in a face-on adsorption orientation. The adsorption orientation relative to the substrate is denoted by solid white and yellow lines. Image Sizes: a) 15.2 × 15.2 nm² b) 4.8 × 4.8 nm². Imaging parameters: a,b) sample bias voltage = -2.7 V, tunneling current = 300 pA.

First, we will examine the behavior of a single, isolated CuPc adsorbed on the MAPbI₃ surface (Fig. 1a). A zoomed-in filled-state image of the CuPc (Fig. 1b) shows eight round outer orbitals, which surround eight smaller, inner orbitals. This intramolecular contrast is indicative of the highest occupied molecular orbital (HOMO) of CuPc, as well as a flat-lying, or “face-on”, adsorption orientation.²⁸ This image also shows the face-on CuPc adsorbed so that its pairs of outer orbitals are aligned along the same [10±1] directions as the I⁻ pairs of the MAPbI₃ substrate (solid white and yellow lines). It was also observed that a single, isolated CuPc molecule can adsorb 45° rotated relative to the halide pairs (Fig. S2). The molecular dimensions of CuPc are such that periodic overlap between the CuPc orbitals and the I⁻ lattice sites is difficult, as discussed later. Additionally, it was found that the face-on adsorbed CuPc

molecule was easily moved by the STM tip (Fig. S3), suggesting a relatively weak molecule-substrate interaction between MAPbI₃ and CuPc.

The face-on adsorbed CuPc molecule was a rare observation, and it was found that CuPc preferentially formed a self-assembled (SA) layer on top of the MAPbI₃ film. In Figure 2a, there are multiple MAPbI₃ grains exhibiting the previously reported paired surface reconstruction.²⁰ In the middle of the image there is a brighter, striped domain, which is attributed to an SA layer of CuPc molecules. A zoomed-in image of one of these domains (Fig. 2b) reveals alternating rows of brighter and darker protrusions. The direction perpendicular to these rows will be referred to as the c-axis of the SA layer. The direction parallel to the bright and dark rows will be referred to as the b-axis. Periodicities of 4.4 ± 0.2 Å along the b-axis and 1.14 ± 0.04 nm along the c-axis were obtained from an average of 17 different SA layers. To interpret these images, it is important to note that CuPc is polymorphic in nature. These polymorphs are characterized both by intermolecular spacings and the so-called stacking angle. Here, the convention used for the stacking angle is the angle (φ) between the CuPc molecular plane and the b-axis of the CuPc SA layer (Fig. 2c). The α-polymorph of CuPc (α-CuPc) features b-axis periodicity of 3.8 Å and a stacking angle of approximately 63°.^{29, 30} The CuPc SA layers measured on MAPbI₃ exhibit periodicity along an angle of 61 ± 2° (red line, Fig. 2b), which is consistent with the α-phase CuPc stacking angle, suggesting that CuPc molecules may also stack at this angle in the observed SA layer. The measured value of 1.14 ± 0.04 nm for the c-axis spacing is slightly lower than, but nearly consistent with, the value of 1.2 nm reported in literature for α-CuPc.^{29, 30} It should also be noted that a wide range of c-axis spacings (1.18 nm-1.69 nm) have been reported for CuPc SA layers on other substrates.³¹⁻³³ Notably, both the c-axis and b-axis periodicities observed here match well the values for a CuPc layer on Bi₂Se₃. Importantly, the b-axis periodicity in these studies is larger than the expected 3.8 Å spacing of α-CuPc, therefore the exact stacking structure may be due to some modification of the α-CuPc structure.

To further evaluate the possible structure and orientation of the CuPc SA layer, simulated STM images were generated *via* DFT for various crystal plane surfaces of α-CuPc. Additionally, the surface energy for each crystal plane surface was calculated using the following equation:

$$E_{surf} = \frac{E_s - E_0}{2 \times S}$$

where E_s and E₀ are the energy of the CuPc molecule structure with and without the surface, and S is the area of the surface. The surface area is multiplied by a factor of two because two symmetric surfaces are introduced due to periodic boundary conditions. The (100) surface of α-CuPc (Fig. 2d) is found to be the most favorable, with a surface energy of 19.09 mJ/mm². All other surfaces have energies over twice as high. Additionally, the low isosurface density value simulated STM image of the (100) surface (Fig. 2e) reproduces well the pattern of alternating rows of bright and dark protrusions observed in the experimental STM images. Also, both the experimental and simulated STM images for the (100) surface show periodicity along a stacking angle of 61-62°, which is consistent with literature values for α-CuPc. The

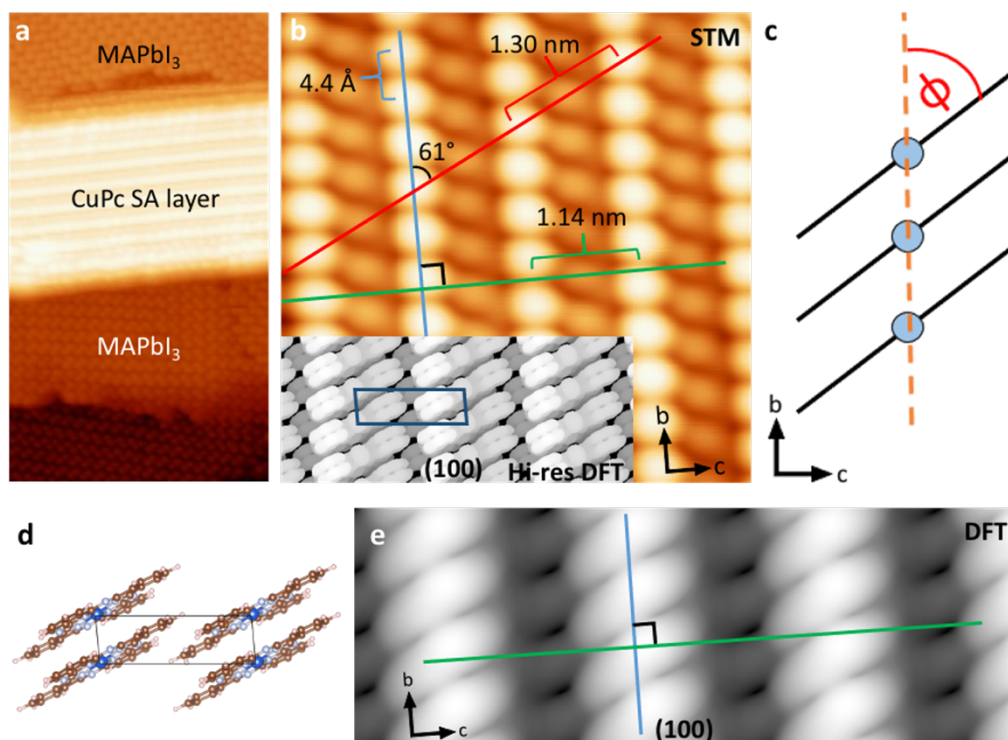


Figure 2. CuPc self-assembled (SA) layer on MAPbI₃. a) Overview STM image showing a CuPc SA layer on top of MAPbI₃. b) Zoom-in STM image of a CuPc SA layer showing the bright-dark alternating rows of protrusions. Colored lines show directions of interest, with correspondingly colored brackets denoting the distance of one period. Angles relative to the b-direction (blue line) along the SA layer are noted. Inset: High isosurface density value (“high resolution”) DFT simulated STM image of the (100) surface of α -CuPc. c) Schematic denoting the CuPc polymorph stacking angle convention used here. d) Crystal structure showing the (100) surface of α -CuPc. e) Low isosurface density value (“low resolution”) DFT simulated STM image of the (100) surface of α -CuPc. Image sizes: a) $16.4 \times 29.7 \text{ nm}^2$ b) $4.5 \times 4.5 \text{ nm}^2$. Imaging parameters: a) sample bias voltage = -2.7 V , tunneling current = 100 pA ; b) sample bias voltage = -2.6 V , tunneling current = 150 pA .

high isosurface density value simulated STM image of the (100) surface shows clearer features of individual atoms in the CuPc molecule and demonstrates how CuPc molecules correspond to the bright and dark protrusions in the experimental image (inset, Fig. 2b). The 1.21 nm periodicity along the c-axis in the simulated image of (100) α -CuPc is nearly consistent with that measured in experiment ($1.14 \pm 0.04 \text{ nm}$). It should also be noted that the (001) and (110) surfaces also qualitatively reproduce the bright-dark alternating rows of protrusions but exhibit much higher surface energies. The surface energies and simulated STM images for the four different crystal planes considered are summarized in Fig. S4. Although the analysis here is based on STM images taken at a negative bias (filled states), an image of the CuPc SA layer taken at positive bias (empty states) has been included for reference (Fig. S5).

The fact that multiple crystal planes provide a qualitative match to the experiment strongly corroborates the hypothesis that an α -CuPc type structure gives rise to the alternating bright and dark rows of protrusions seen in the STM images. A detailed comparison of the simulated STM images with different isosurface density values shows how CuPc stacking can give rise to the bright-dark pattern seen in experiment (Fig. S6). High isosurface density value images show a surface with high electron density, closer to the individual atomic cores, whereas low isosurface density value images show a surface with low electron density, indicative of overall molecular size or shape. The (100) α -CuPc surface is the most promising candidate, but the exact orientation of the CuPc molecules is not discernable from these results since the simulation and experiment are not an exact match. Periodicity along a 62° angle relative to the b-axis in the simulated image of the (100) surface matches experimental data well and is consistent with the expected stacking angle

for α -CuPc. However, in the simulated image the c-axis (green line, Fig. 2e) intersects the bright protrusions, in a different fashion than in the experimental image (green line, Fig. 2b). Thus, the exact stacking structure likely differs slightly from the structures determined *via* simulation. Testing alternate structures with longer range periodicity was not feasible due to computational expense. It is also important to note that these simulations of α -CuPc were performed in gas phase, not accounting for the MAPbI₃ substrate. Thus, it is possible the substrate could impose some restrictions on molecular orientation and stacking, causing it to differ slightly from the α -CuPc gas phase simulations.

To gain additional clues regarding the orientation of CuPc molecules, height measurements of the SA layer were taken (Fig. S7). Since measured apparent heights in STM images are a convolution of geometric position and local density of states, the values can vary depending on the gap voltage used during imaging. An average CuPc SA layer height of $9.0 \pm 0.7 \text{ \AA}$ was obtained from measurements of 13 different CuPc SA layers. Slightly different voltages were used for some of the images included in the above average, which may contribute to the variance. For comparison, when averaging height measurements of 6 SA layers all imaged at the same sample bias voltage of -2.7 V , a value of $8.6 \pm 0.5 \text{ \AA}$ was obtained. In both cases, the height value is significantly less than the 1.4-1.9 nm layer height expected if CuPc molecules are adsorbed edge-on.^{28,32} The measured SA layer height is also less than the measured molecular width of CuPc (Fig. S8), which gives a first approximation of the apparent step height of the SA layer if the molecule were adsorbed edge-on. This implies two possibilities: 1) the CuPc molecules are adsorbed edge-on, but the measured apparent height is strongly influenced by electronic effects or 2) the measured value does

represent the true physical height of the SA layer but the CuPc molecules are adsorbed at some tilt angle, θ , relative to the MAPbI₃ film. Here, θ can be approximated using the STM measured values and basic trigonometric relations (see Fig. S7c for details), and an estimated tilt angle of 24° was found. Some non-zero tilt angle relative to the substrate could also potentially explain the deviation of the b-axis spacing we observed with respect to the literature values for stand-alone α -CuPc.

Further hints of the stacking structure were gleaned from the zig-zag shape of the SA layer's supramolecular structure, which features bends of $121 \pm 2^\circ$ (Fig. 3a). There is no apparent threshold width or length of the SA layer above which these bends occur. It is worth noting that deposition trials of CuPc on MAPbBr₃ were performed and qualitatively similar results were obtained (Fig. S9), suggesting that the halide in the X position of the perovskite is not of critical importance to CuPc adsorption behavior. Similar bends have also been previously reported for CuPc on Bi(111),³¹ but it is not clear what triggers these bends to occur. However, the fact that the angle of the bend is approximately twice the stacking angle of α -phase CuPc suggests that the bend occurs due to the border of two domains of α -CuPc.

Evidence supporting this hypothesis was found by looking at defects in the SA layer near one of these bends (Fig. 3b). The defects occur as pairs of depressions, with one depression in a bright row (dashed yellow circles) and an accompanying depression in the adjacent darker row (dashed green circles). However, the orientation of these pairs is different on each side of the bend. On the top right side of the bend, the accompanying depressions in the darker row are positioned above and to the left of the depressions in the bright row. In contrast, on the lower left side of the bend the relative position of the paired defects, which are being tentatively interpreted as a missing CuPc molecule, is flipped. We propose that the bend depicted in Fig. 3 is observed when two α -CuPc domains meet in an offset fashion at the bend itself (white/brown two-tone rectangles, Fig. 3b). Additionally, if the two bends shown in Figures 3a and 3b are compared closely, it is evident that there is a different arrangement occurring at each bend. In Figure 3b the bright and dark rows on each side of the bend line up with each other,

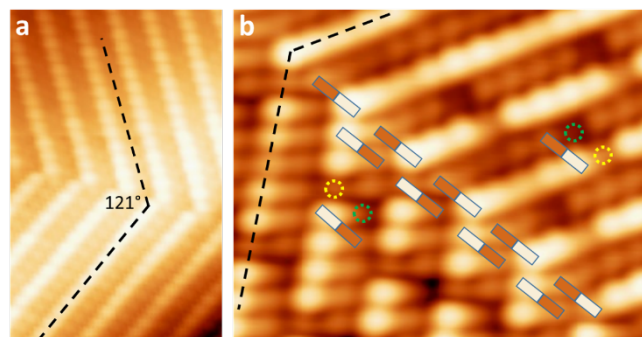


Figure 3. Defects at a bend in the CuPc SA layer. a) STM image of a macroscopic bend in the CuPc SA layer. Dashed black lines denote the angle of the bend. Note that the bright and dark rows are offset at the bend. b) STM image of paired defects occurring near a bend in the CuPc SA layer. Depressions in the bright and dark rows are denoted by dashed green and yellow circles, respectively. The two-tone rectangles denote one CuPc molecule and are shown at the bend to highlight that the two domains are offset by half of a molecule. Note that the bright and dark rows line up at the bend. Image size: a) $6.6 \times 10.3 \text{ nm}^2$ b) $6.1 \times 4.8 \text{ nm}^2$. Imaging parameters: a) sample bias voltage = -2.5 V, tunneling current = 60 pA b) sample bias voltage = -2.6 V, tunneling current = 52 pA.

whereas in Figure 3a they are offset from each other. For that offset row case, the CuPc arrangement is similar to Figure 3b, except the relative position of the molecules on each side of the bend are shifted by half of a molecule. The SA layers were found to follow a Volmer-Weber, or “island”, growth pattern, in which the 2nd layer begins to grow before a complete first layer is formed (Fig. S10). The 2nd layer shows the same bright-dark alternating row structure as the 1st layer. This suggests that the structure adopted by the 1st layer is not strongly affected by the underlying MAPbI₃ film, providing evidence of weak CuPc SA layer-MAPbI₃ interaction. This idea is further supported by the observation that CuPc SA layers can cross unperturbed over MAPbI₃ grain boundaries (Fig. S11). Additionally, a survey of STM images reveals that numerous relative angles between the CuPc SA layer and the MAPbI₃ are possible, further indicating a weak interaction (Fig. S12).

To evaluate the CuPc-MAPbI₃ interaction and better understand CuPc SA layer formation from a theoretical perspective, DFT calculations of a CuPc molecule on top of MAPbI₃ were performed (Fig 4). It should be noted that the CuPc for these calculations is forced to match the periodicity of the MAPbI₃ to reduce computational costs. Thus, these do not reflect the α -CuPc structures but are used as a basic model to gain insight into molecule-substrate interactions. Two different edge-on adsorption scenarios, single and double isoindole group adsorption, were modeled and compared with the system energy of a face-on adsorption. For each case, dE values for the CuPc-MAPbI₃ systems were calculated using the formula:

$$dE = E - E_{\text{bulk}}(\text{CuPc}) - E_{\text{surf}}(\text{MAPbI}_3)$$

where E is the total system energy, $E_{\text{bulk}}(\text{CuPc})$ is the energy of bulk α -CuPc, and $E_{\text{surf}}(\text{MAPbI}_3)$ is the energy of the $\sqrt{2} \times \sqrt{2}$ MAPbI₃ supercell (Fig. 4). Physically, dE represents the energy gain or loss when putting CuPc in contact with the MAPbI₃ perovskite surface. The first important result is that the face-on adsorption is lower in energy than both the single and double isoindole edge-on adsorption cases. This is consistent with a previously reported calculation¹⁷ and also agrees with the experimental STM images reported here showing that a single, isolated CuPc molecule adsorbs on MAPbI₃ in a face-on orientation (Fig. 1). The higher energy for the edge-on CuPc simulations is somewhat surprising considering the predominant SA layers seen in the experimental STM images show characteristics of edge-on adsorption. This can be explained by the fact that the CuPc in the computations is forced to match MAPbI₃ periodicity. This results in CuPc molecules that are much further away from each other than they would be in α -phase CuPc (e.g., neighboring CuPc can be considered as weakly- or non-interacting). Consequently, the energetically beneficial π - π orbital stacking

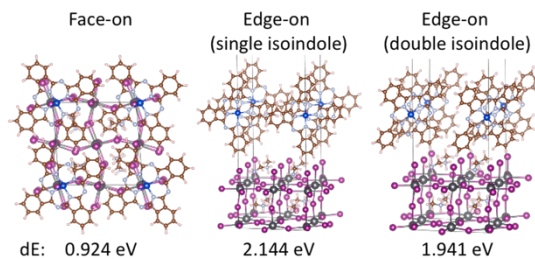


Figure 4 DFT computations of the CuPc-MAPbI₃ interface. Model of face-on (a) and edge-on single- (b) and double- (c) isoindole adsorption cases. dE values given are calculated using bulk α -CuPc as a reference state.

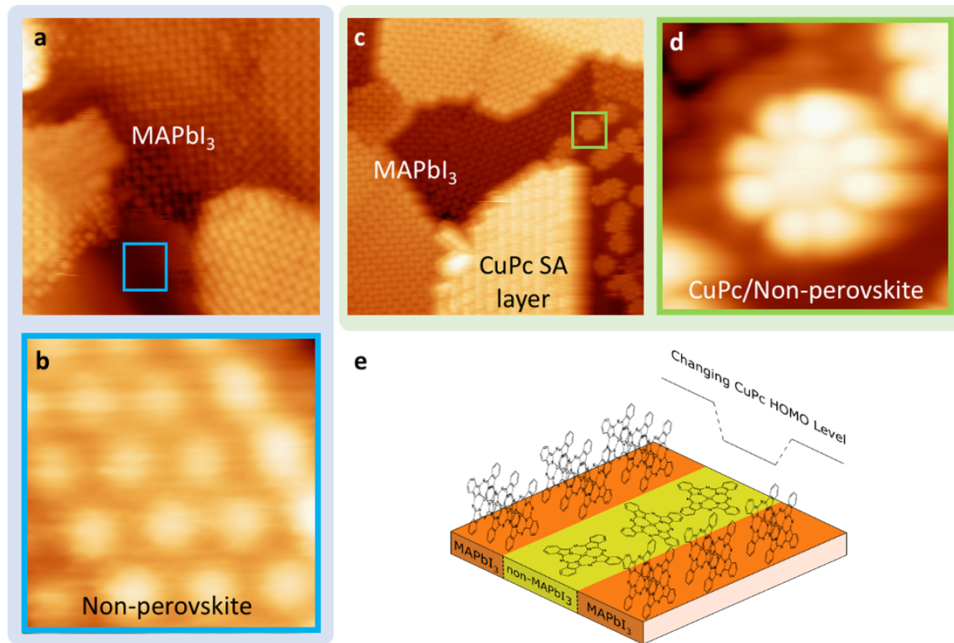


Figure 5 Non-perovskite domain and corresponding CuPc behavior. CuPc adsorption on non-MAPbI₃ surface. a) Overview STM image showing a MAPbI₃ film before CuPc deposition. The bottom of the image features a smooth, featureless area. b) Zoom-in of the blue box area from (a) revealing atomic corrugation with a hexagonal pattern and a lattice constant of approximately 4.3 Å. c) A similar area featuring MAPbI₃ and non-MAPbI₃ domains after CuPc deposition. Very different behavior of CuPc molecules is seen depending on the domain where it is adsorbed (*i.e.*, perovskite or not). d) Zoom-in of face-on adsorbed CuPc on the non-MAPbI₃ domain. e) Schematic of the CuPc interfacial layer disrupted by a non-perovskite domain and the possible change in the CuPc HOMO level. Image sizes: a) 17.6 × 17.6 nm² b) 1.6 × 1.6 nm²; c) 26.4 × 26.4 nm²; d) 3.3 × 3.3 nm². Imaging parameters: a,c-d) sample bias voltage = -2.5 V, tunneling current = 100 pA; b) sample bias voltage = -2.2 V, tunneling current = 100 pA.

present in α -CuPc is not accurately taken into account in these calculations, providing a rationale for the lower dE energy estimated here for the face-on configuration with respect to the edge-on configuration. The models of Figure 4 suggest that molecule-molecule interaction must be considered to explain the formation of the CuPc SA layer depicted earlier, where molecules were placed in the edge-on configuration. A particular stacking angle of the CuPc that maximizes intermolecular interaction is necessary to compensate for the lower stability calculated for isolated (*e.g.*, non-interacting) edge-on CuPc with respect to a face-on molecule. The combined experimental and theoretical results suggest that the CuPc intermolecular forces are stronger than the CuPc-MAPbI₃ interaction. It is important to reiterate that the simulated STM images, which match experimental images of the SA layer, are for α -CuPc in the gas phase. Thus, CuPc on MAPbI₃ largely resembles α -CuPc on its own, implying a very weak effect from the perovskite substrate. Considering this weak interaction in the extreme case, the energy of the CuPc SA layer-MAPbI₃ system could be approximated by the sum of the energy of the two separated systems. The fact that the dE values are positive for every case means that the simulated interface is higher in energy than the sum of the bulk α -CuPc and MAPbI₃ reference state (Fig. 4). Using the approximation proposed above, the positive dE values mean that the CuPc SA layer-MAPbI₃ system is more energetically favorable than the simulated scenarios, further supporting the importance of intermolecular interaction in the stabilization of the SA layer recorded in the STM experiment.

The MAPbI₃ thin film samples featured some domains of non-perovskite material, and it was observed that CuPc behaves differently on these non-perovskite domains. In Figure 5a, an image of the MAPbI₃ surface shows the expected perovskite surface reconstruction except for a small area where no apparent corrugation is observed (blue square). A closer look at this area in Figure 5b reveals atomic corrugation with a hexagonal pattern and a lattice constant of 4.3 Å. The right side of Figure 5c shows how CuPc interacts with the unknown, non-MAPbI₃ surface. In stark contrast to MAPbI₃, on the non-perovskite domains there are numerous CuPc molecules face-on adsorbed in a disordered fashion,

and in close proximity to each other. A zoomed-in image shows the HOMO of an individual CuPc on this unknown material, as evidenced by the eight outer orbital lobes (Fig. 5d). The fact that CuPc molecules in close proximity are able to maintain a flat-lying orientation without clear ordering, rather than forming an SA layer, indicates that the molecule-substrate interaction with the non-perovskite material is stronger than with MAPbI₃ and can compete with SA layer formation. This behavior is particularly striking considering that there is an SA layer extremely close to the individual CuPc molecules. It is also worth noting that the MAPbI₃ surface in Figure 5c is completely devoid of individual, face-on CuPc molecules. This difference in behavior has important implications for the perovskite-HTL interface in devices that have a nonstoichiometric perovskite film. Different adsorption geometries would have a dramatic effect on the orbital overlap between the CuPc and MAPbI₃. Additionally, reports have shown orientation dependent changes in the ionization potential and interfacial energy level alignment for CuPc, attributed to the C-H surface dipole present in an edge-on orientation.³⁴ Such changes in the CuPc HOMO level (Fig. 5e) would affect energy level alignment at the interface of an MHP-based device and can be expected to significantly alter interfacial charge transfer and overall device performance.

The identity of the non-perovskite domain cannot be completely determined from the STM images alone, but some candidates can be identified based on the lattice structure and spacing. A reasonable hypothesis is that these non-perovskite domains are excess precursor material, either PbI₂ or MAI. Literature shows that PbI₂ forms a hexagonal lattice with nearest neighbor spacing ranging from 4.5-4.6 Å.^{35, 36} The hexagonal structure on the non-perovskite domains was 4.3 Å, consistent with literature within STM measurement uncertainty. Therefore, PbI₂ is considered to be a viable candidate for the non-perovskite domain. For the other precursor, MAI, a tetragonal unit cell is expected,³⁷ which is not consistent with the hexagonal lattice of the non-perovskite domain. Based on this interpretation, MAI was eliminated as a candidate for the non-MAPbI₃ domains observed. She *et al.* reported a hexagonal pattern after deposition of MAI on Au(111),

and explained the result as iodine atoms leftover after MAI dissociates upon reacting with the metal Au(111) surface.³⁵ This explanation is also feasible for the result obtained in this study. Evidence supporting this hypothesis was found in STM images of a non-optimized MAPbI₃ deposition trial, in which only approximately 30% of the sample surface was perovskite. The non-perovskite domain featured a hexagonal superstructure with a spacing of 2.61 nm that was rotated 9° relative to the 4.3 Å atomic hexagonal lattice (Fig. S13). The superstructure spacing is somewhat larger than previous reports, but the atomic lattice spacing and relative degree of rotation match well previous reports of iodine adlayers.^{38, 39} Based on this, the non-perovskite domain could potentially be an iodine adlayer. Overall, evidence was found supporting both PbI₂ and an iodine adlayer as the identity of the non-perovskite domains. Pb and bare Au(111) were also considered and eliminated as possibilities. The rationale for these eliminations is described in a Supplemental Note.

Utilization of excess precursor has been reported in the literature as having a strong influence on perovskite film quality, device performance and stability. For example, excess PbI₂ has been shown to be beneficial in small amounts, but detrimental above a threshold value.⁴⁰ Our study highlights a complication that can occur even with small, nanometer scale domains of non-perovskite material. Namely, changes in composition of the perovskite film can cause secondary effects on the adsorption geometry and continuity of organic thin film HTLs. This change in interfacial orientation affects energy level alignment, charge transfer, and, ultimately, device performance. As can be seen in Figure Sd, a nanometer scale domain of non-perovskite material can cause a disruption in the ordered formation of the HTL. Although the results of this study were obtained at low temperatures, we have observed the same perovskite surface reconstruction *via* STM in the tetragonal and cubic phase temperature ranges in which real-world perovskite solar cells are typically characterized and operated. Additionally, the α -CuPc phase used as the basis of the DFT simulations has been characterized in the literature using XRD and TED measurements taken at room temperature.³⁰ Therefore, the CuPc/perovskite interfacial behavior observed here is also expected to hold for real-world devices. Understanding how, even at the currently recommended low levels of excess PbI₂, these non-perovskite domains in nonstoichiometric perovskite films interact with potential HTL layers is essential for accurately predicting interfacial properties. The confounding effects such discontinuity at the interface has on charge transfer, performance and stability is of prime importance for optimizing the use of excess precursor to further improve perovskite device technology.

CONCLUSION

Utilizing a combined STM and DFT study, we shine the light on the atomic structure of the CuPc/MAPbI₃ interface. The CuPc/MAPbI₃ film was used as a model system for understanding how non-stoichiometric perovskite films could affect the perovskite/HTL interface structure, and potentially its electronic properties. Scanning tunneling microscopy reveals that the first interfacial layer of CuPc does not adsorb face-on to MAPbI₃, but instead forms a self-assembled layer that features a structure similar to the α -polymorph of CuPc. A similar result was found for CuPc on MAPbBr₃, suggesting that changing the halide in the X position does not significantly alter the CuPc-MAPbX₃ interfacial structure. In contrast, CuPc behaved differently on non-perovskite domains in the film, adsorbing in a face-on orientation. The orientation of the CuPc molecule has been shown to affect interface energetics, thus this behavior shows how non-stoichiometric ratios in perovskite films can affect interface structure and charge transfer at the HTL/MHP interface in MHP-based devices. This work underscores the importance of understanding the exact structure of

interfaces in MHP devices to properly predict device performance and rationally design perovskite devices.

METHODS

Surface characterization. Optimized MAPbI₃ films were prepared in UHV by co-evaporation of PbI₂ and MAI at 513 K and 378 K, respectively, for 5 minutes onto a cleaned Au(111) substrate held at 130 K. Two K-cells containing the respective precursor materials, PbI₂ and MAI, were gradually heated from room temperature to the desired deposition temperature over a period of approximately 120-180 min. Power applied to the K-cells was manually adjusted until the thermocouples on the K-cells had stable readouts of the desired deposition temperatures for at least 5 minutes. The sample was then introduced into the deposition chamber. Once the sample was in position, the shutters of the K-cells were opened to begin deposition. The deposition rate of PbI₂ was monitored using a quartz crystal microbalance, with a typical deposition rate of 0.01-0.02Å/s. Slower deposition rates were found to be beneficial for producing uniform films. Due to the non-directional nature of MAI evaporation, the rate could not be accurately monitored by QCM.^{41, 42} After achieving a desirably slow PbI₂ deposition rate, XPS survey scans were used to evaluate sample composition and determine necessary adjustments to the power of the K-cell filled with MAI. The I:Pb peak height ratio, as well as the presence and height of C and N peaks were used as guides for adjusting the MAI K-cell's power for the next deposition. Higher MAI temperature during deposition led to the non-stoichiometric films with larger non-perovskite domains, possibly due to MAI decomposition during deposition. Preparation of these non-optimized films was carried out using the same protocols as the optimized films except using deposition temperatures of T_{PbI₂} = 521 K and T_{MAI} = 397 K. Samples were annealed at room temperature for at least 3 hours before being transferred into the STM setup. After the success of the perovskite deposition was confirmed *via* STM imaging, the sample was transferred in UHV to a preparation chamber where CuPc was deposited onto the perovskite sample. The commercial CuPc powder (Sigma Aldrich, triple sublimated grade) was further purified by vacuum sublimation *in situ* before performing any depositions. CuPc was deposited *via* vacuum sublimation using a K-cell at 638 K for an initial duration of 30 s. Additional CuPc (up to 190 s of cumulative deposition) was incrementally deposited to explore higher coverages. The perovskite/Au(111) substrate was held at room temperature during this deposition, and the sample was transferred to the STM chamber without any further treatment. During CuPc deposition, the chamber pressure was 6×10^{-8} torr. Narrow-mouthed crucibles were used, and a shutter was used to prevent unintended deposition onto the sample during transfer within the preparation chamber. To prevent a blocking layer of re-condensed CuPc near the top of the crucible, CuPc was filled almost to the top of the crucible. Additionally, the K-cell shutter was left open during temperature ramping so that any material sublimated during temperature ramping would not collect near the mouth of the crucible. The shutter was only closed for the 2-3 minutes immediately before deposition, while the sample was being transferred into the deposition chamber. All STM imaging was performed at 4.5 K. For MAPbBr₃ films, PbBr₂ and MABr were co-evaporated at 533 K and 376 K, respectively, for 4 minutes onto a cooled Au(111) substrate held at 150 K.

Density functional theory. In this study, the DFT calculations were performed using the Vienna *ab Initio* simulation package (VASP).⁴³ The projector augmented wave approach⁴⁴ was employed using a plane wave basis set with an energy cutoff of 500 eV. The generalized gradient approximation (GGA) with the Perdew-Burke-Ernzerhof (PBE) exchange-correlation functional⁴⁵ was used to evaluate the exchange-correlation energy. In all calculations, the total energy of system was converged within 10⁻⁶ eV. In CuPc bulk calculations, a cell containing one molecule of CuPc was used, and for MAPbI₃ calculations a supercell containing four molecules of MAPbI₃ was used. Brillouin zone sampling was done using 3×9×3 and 4×4×4 Monkhorst-Pack k-point grids⁴⁶ centered at the Gamma point in the CuPc and MAPbI₃ bulk crystal calculations, respectively. For CuPc crystal surface calculations, a 3×9×1 Monkhorst-Pack k-point grid was used and a vacuum region of 12 Å was added in the direction normal to the surface. Slab cells were used to model CuPc stacking on top of the MAPbI₃ substrate, with

a vacuum region of 26 Å in the direction normal to the stacking plane to minimize the effect of periodic images. A Monkhorst-Pack k-point grid of 3×3×1 was used for these slab models. All the structures were fully relaxed until the residual force acting on each atom was lower than 0.01 eV/Å.

ASSOCIATED CONTENT

Supporting Information:

Figs. S1-S11 providing information on face-on CuPc adsorption angle, movement of CuPc by STM tip, simulated images of various α -CuPc crystal planes using different isos density values, SA layer height measurements, CuPc molecular width measurements, CuPc SA layers on MAPbBr₃, 2nd layer CuPc growth, CuPc SA layer crossing perovskite grain boundaries, relative angles of CuPc SA layer and MAPbI₃, and hexagonal superstructure of the non-perovskite domain. Supplemental Note 1 describes rationale for eliminating Pb and Au(111) as the identity of the non-perovskite domain.

This material is available free of charge *via* the internet at <http://pubs.acs.org>.

AUTHOR INFORMATION

Corresponding Authors

* Yabing Qi, Yabing.Qi@OIST.jp

* Guofeng Wang, guw8@pitt.edu

Present Addresses

† Scanning Probe Microscopy Laboratory, Physics and Materials Science Research Unit, University of Luxembourg, Luxembourg.

ORCID IDs

Collin Stecker: 0000-0003-4247-5699

Jeremy Hieuille: 0000-0003-4891-4007

Luis K. Ono: 0000-0003-3176-1876

Yabing Qi: 0000-0002-4876-8049

Author Contributions

‡ C.S. and Z.L. contributed equally.

Notes

The authors declare no competing financial interest.

ACKNOWLEDGMENT

This work was supported by funding from the Energy Materials and Surface Sciences Unit of the Okinawa Institute of Science and Technology Graduate University, the OIST R&D Cluster Research Program, the OIST Proof of Concept (POC) Program, JSPS KAKENHI Grant Number JP18K05266, and JST A-STEP Grant Number JPMJTM20HS, Japan. G. Wang gratefully acknowledges the computational resources provided by the University of Pittsburgh Center for Research Computing as well as the Extreme Science and Engineering Discovery Environment (XSEDE).

REFERENCES

- (1) *Best Research-Cell Efficiency Chart*; National Renewable Energy Laboratory (NREL). <https://www.nrel.gov/pv/assets/pdfs/best-research-cell-efficiencies.20200104.pdf> (accessed May 10th, 2021).
- (2) Yang, Y., Yang, M., Moore, David T., Yan, Y., Miller, Elisa M., Zhu, K. and Beard, Matthew C. Top and Bottom Surfaces Limit Carrier Lifetime in Lead Iodide Perovskite Films. *Nat. Energy* **2017**, *2*, 16207.

- (3) Schulz, P., Cahen, D. and Kahn, A. Halide Perovskites: Is It All About the Interfaces? *Chem. Rev.* **2019**, *119*, 3349-3417.
- (4) Qiu, L. B., Ono, L. K., Jiang, Y., Leyden, M. R., Raga, S. R., Wang, S. H. and Qi, Y. B. Engineering Interface Structure to Improve Efficiency and Stability of Organometal Halide Perovskite Solar Cells. *J. Phys. Chem. B* **2018**, *122*, 511-520.
- (5) Wu, Z. F., Liu, Z. H., Hu, Z. H., Hawash, Z., Qiu, L. B., Jiang, Y., Ono, L. K. and Qi, Y. B. Highly Efficient and Stable Perovskite Solar Cells *via* Modification of Energy Levels at the Perovskite/Carbon Electrode Interface. *Adv. Mater.* **2019**, *31*, 1804284.
- (6) Wu, Z. F., Jiang, M. W., Liu, Z. H., Jamshaid, A., Ono, L. K. and Qi, Y. B. Highly Efficient Perovskite Solar Cells Enabled by Multiple Ligand Passivation. *Adv. Energy Mater.* **2020**, *10*, 1903696.
- (7) Emará, J., Schnier, T., Pourdavoud, N., Riedl, T., Meerholz, K. and Olthof, S. Impact of Film Stoichiometry on the Ionization Energy and Electronic Structure of CH₃NH₃PbI₃ Perovskites. *Adv. Mater.* **2016**, *28*, 553-559.
- (8) Chen, Q., Zhou, H., Song, T. B., Luo, S., Hong, Z., Duan, H. S., Dou, L., Liu, Y. and Yang, Y. Controllable Self-Induced Passivation of Hybrid Lead Iodide Perovskites toward High Performance Solar Cells. *Nano Lett.* **2014**, *14*, 4158-4163.
- (9) Hawash, Z., Raga, S. R., Son, D.-Y., Ono, L. K., Park, N.-G. and Qi, Y. Interfacial Modification of Perovskite Solar Cells Using an Ultrathin MAI Layer Leads to Enhanced Energy Level Alignment, Efficiencies, and Reproducibility. *J. Phys. Chem. Lett.* **2017**, 3947-3953.
- (10) Arora, N., Dar, M. I., Hinderhofer, A., Pellet, N., Schreiber, F., Zakeeruddin, S. M. and Gratzel, M. Perovskite Solar Cells with CuSCN Hole Extraction Layers Yield Stabilized Efficiencies Greater Than 20%. *Science* **2017**, *358*, 768-771.
- (11) Jiang, X., Wang, D., Yu, Z., Ma, W., Li, H.-B., Yang, X., Liu, F., Hagfeldt, A. and Sun, L. Molecular Engineering of Copper Phthalocyanines: A Strategy in Developing Dopant-Free Hole-Transporting Materials for Efficient and Ambient-Stable Perovskite Solar Cells. *Adv. Energy Mater.* **2019**, *9*, 1803287.
- (12) Cheng, M., Li, Y. Y., Safdari, M., Chen, C., Liu, P., Kloo, L. and Sun, L. C. Efficient Perovskite Solar Cells Based on a Solution Processable Nickel (II) Phthalocyanine and Vanadium Oxide Integrated Hole Transport Layer. *Adv. Energy Mater.* **2017**, *7*, 1602556.
- (13) Yang, G., Wang, Y. L., Xu, J. J., Lei, H. W., Chen, C., Shan, H. Q., Liu, X. Y., Xu, Z. X. and Fang, G. J. A Facile Molecularly Engineered Copper (II) Phthalocyanine as Hole Transport Material for Planar Perovskite Solar Cells with Enhanced Performance and Stability. *Nano Energy* **2017**, *31*, 322-330.
- (14) Cho, K. T., Trukhina, O., Roldan-Carmona, C., Ince, M., Gratia, P., Grancini, G., Gao, P., Marszalek, T., Pisula, W., Reddy, P. Y., Torres, T. and Nazeeruddin, M. K. Molecularly Engineered Phthalocyanines as Hole-Transporting Materials in Perovskite Solar Cells Reaching Power Conversion Efficiency of 17.5%. *Adv. Energy Mater.* **2017**, *7*, 1601733.
- (15) Wang, J. M., Wang, Z. K., Li, M., Zhang, C. C., Jiang, L. L., Hu, K. H., Ye, Q. Q. and Liao, L. S. Doped Copper Phthalocyanine *via* an Aqueous Solution Process for Normal and Inverted Perovskite Solar Cells. *Adv. Energy Mater.* **2018**, *8*, 1701688.
- (16) Zhang, X. F., Zhou, X. Y., Zhang, L. Z. and Xu, B. M. Facile Phthalocyanine Doping into PEDOT Leads to Highly Efficient and Stable Inverted Metal Halide Perovskite Solar Cells. *J. Mater. Chem. A* **2018**, *6*, 12515-12522.
- (17) Kim, Y. C., Yang, T. Y., Jeon, N. J., Im, J., Jang, S., Shin, T. J., Shin, H. W., Kim, S., Lee, E., Kim, S., Noh, J. H., Seok, S. I. and Seo, J. Engineering Interface Structures between Lead Halide Perovskite and Copper Phthalocyanine for Efficient and Stable Perovskite Solar Cells. *Energy Environ. Sci.* **2017**, *10*, 2109-2116.
- (18) Zhang, F. G., Yang, X. C., Cheng, M., Wang, W. H. and Sun, L. C. Boosting the Efficiency and the Stability of Low Cost

Perovskite Solar Cells by Using CuPc Nanorods as Hole Transport Material and Carbon as Counter Electrode. *Nano Energy* **2016**, *20*, 108-116.

(19) He, S. S., Qiu, L. B., Son, D. Y., Liu, Z. H., Juarez-Perez, E. J., Ono, L. K., Stecker, C. and Qi, Y. B. Carbon-Based Electrode Engineering Boosts the Efficiency of All Low-Temperature Processed Perovskite Solar Cells. *ACS Energy Lett.* **2019**, *4*, 2032-2039.

(20) She, L. M., Liu, M. Z. and Zhong, D. Y. Atomic Structures of CH₃NH₃PbI₃ (001) Surfaces. *ACS Nano* **2016**, *10*, 1126-1131.

(21) Ohmann, R., Ono, L. K., Kim, H. S., Lin, H., Lee, M. V., Li, Y., Park, N. G. and Qi, Y. B. Real-Space Imaging of the Atomic Structure of Organic-Inorganic Perovskite. *J. Am. Chem. Soc.* **2015**, *137*, 16049-16054.

(22) Hsu, H. C., Huang, B. C., Chin, S. C., Hsing, C. R., Nguyen, D. L., Schnedler, M., Sankar, R., Dunin-Borkowski, R. E., Wei, C. M., Chen, C. W., Ebert, P. and Chiu, Y. P. Photodriven Dipole Reordering: Key to Carrier Separation in Metalorganic Halide Perovskites. *ACS Nano* **2019**, *13*, 4402-4409.

(23) Stecker, C., Liu, K. X., Hieulle, J., Ohmann, R., Liu, Z. Y., Ono, L. K., Wang, G. F. and Qi, Y. B. Surface Defect Dynamics in Organic-Inorganic Hybrid Perovskites: From Mechanism to Interfacial Properties. *ACS Nano* **2019**, *13*, 12127-12136.

(24) Hieulle, J., Wang, X. M., Stecker, C., Son, D. Y., Qu, L. B., Ohmann, R., Ono, L. K., Mugarza, A., Yan, Y. F. and Qi, Y. B. Unraveling the Impact of Halide Mixing on Perovskite Stability. *J. Am. Chem. Soc.* **2019**, *141*, 3515-3523.

(25) Hieulle, J., Luo, S. L., Son, D. Y., Jamshaid, A., Stecker, C., Liu, Z. H., Na, G. R., Yang, D. W., Ohmann, R., Ono, L. K., Zhang, L. J. and Qi, Y. B. Imaging of the Atomic Structure of All-Inorganic Halide Perovskites. *J. Phys. Chem. Lett.* **2020**, *11*, 818-823.

(26) Schulz, F., Ijas, M., Drost, R., Hamalainen, S. K., Harju, A., Seitsonen, A. P. and Liljeroth, P. Many-Body Transitions in a Single Molecule Visualized by Scanning Tunnelling Microscopy. *Nat. Phys.* **2015**, *11*, 229-234.

(27) Mugarza, A., Krull, C., Robles, R., Stepanow, S., Ceballos, G. and Gambardella, P. Spin Coupling and Relaxation inside Molecule-Metal Contacts. *Nat. Commun.* **2011**, *2*, 490.

(28) Uhlmann, C., Swart, I. and Repp, J. Controlling the Orbital Sequence in Individual Cu-Phthalocyanine Molecules. *Nano Lett.* **2013**, *13*, 777-780.

(29) Law, K. Y. Organic Photoconductive Materials: Recent Trends and Developments. *Chem. Rev.* **1993**, *93*, 449-486.

(30) Hoshino, A. T., Y.; Miyaji, H. Redetermination of the Crystal Structure of α -Copper Phthalocyanine Grown on KCl. *Acta Cryst.* **2003**, *B59*, 393-403.

(31) Gardener, J., Owen, J. H. G., Miki, K. and Heutz, S. A Scanning Tunnelling Microscopy Investigation into the Initial Stages of Copper Phthalocyanine Growth on Passivated Silicon Surfaces. *Surf. Sci.* **2008**, *602*, 843-851.

(32) Sun, K., Tao, M.-L., Tu, Y.-B. and Wang, J.-Z. Off-Center Rotation of CuPc Molecular Rotor on a Bi(111) Surface and the Chiral Feature. *Molecules* **2017**, *22*, 740.

(33) Sk, R., Mulani, I. and Deshpande, A. Emergent Properties of the Organic Molecule-Topological Insulator Hybrid Interface: Cu-Phthalocyanine on Bi₂Se₃. *J. Phys. Chem. C* **2018**, *122*, 22996-23001.

(34) Chen, W., Qi, D. C., Huang, H., Gao, X. Y. and Wee, A. T. S. Organic-Organic Heterojunction Interfaces: Effect of Molecular Orientation. *Adv. Funct. Mater.* **2011**, *21*, 410-424.

(35) She, L. M., Liu, M. Z., Li, X. L., Cai, Z. Y. and Zhong, D. Y. Growth and Interfacial Structure of Methylammonium Lead Iodide Thin Films on Au(111). *Surf. Sci.* **2017**, *656*, 17-23.

(36) Yang, C.-H., Yau, S.-L., Fan, L.-J. and Yang, Y.-W. Deposition of Lead Iodide Films on Rh(100) Electrodes from Colloidal Solutions—The Effect of an Iodine Adlayer. *Surf. Sci.* **2003**, *540*, 274-284.

(37) Hendricks, S. B. The Crystal Structures of the Monomethyl Ammonium Halides. *Z. Krist.-Cryst. Mater.* **1928**, *67*, 106-118.

(38) Haiss, W., Sass, J. K., Gao, X. and Weaver, M. J. Iodine Adlayer Structures on Au(111) as Discerned by Atomic-Resolution Scanning Tunnelling Microscopy: Relation to Iodide Electrochemical Adsorption. *Surf. Sci.* **1992**, *274*, L593-L598.

(39) Gao, X. and Weaver, M. J. Probing Redox-Induced Molecular Transformations by Atomic-Resolution Scanning Tunneling Microscopy: Iodide Adsorption and Electrooxidation on Gold(111) in Aqueous Solution. *J. Am. Chem. Soc.* **1992**, *114*, 8544-8551.

(40) Roose, B., Dey, K., Chiang, Y. H., Friend, R. H. and Stranks, S. D. Critical Assessment of the Use of Excess Lead Iodide in Lead Halide Perovskite Solar Cells. *J. Phys. Chem. Lett.* **2020**, *11*, 6505-6512.

(41) Ono, L. K., Wang, S. H., Kato, Y., Raga, S. R. and Qi, Y. B. Fabrication of Semi-Transparent Perovskite Films with Centimeter-Scale Superior Uniformity by the Hybrid Deposition Method. *Energy Environ. Sci.* **2014**, *7*, 3989-3993.

(42) Wang, S. H., Ono, L. K., Leyden, M. R., Kato, Y., Raga, S. R., Lee, M. V. and Qi, Y. B. Smooth Perovskite Thin Films and Efficient Perovskite Solar Cells Prepared by the Hybrid Deposition Method. *J. Mater. Chem. A* **2015**, *3*, 14631-14641.

(43) Kresse, G. and Furthmüller, J. Efficient Iterative Schemes for *ab Initio* Total-Energy Calculations Using a Plane-Wave Basis Set. *Phys. Rev. B* **1996**, *54*, 11169-11186.

(44) Kresse, G. and Joubert, D. From Ultrasoft Pseudopotentials to the Projector Augmented-Wave Method. *Phys. Rev. B* **1999**, *59*, 1758-1775.

(45) Perdew, J. P., Burke, K. and Ernzerhof, M. Generalized Gradient Approximation Made Simple. *Phys. Rev. Lett.* **1996**, *77*, 3865-3868.

(46) Monkhorst, H. J. and Pack, J. D. Special Points for Brillouin-Zone Integrations. *Phys. Rev. B* **1976**, *13*, 5188-5192.

TOC:

HTL disruption by non-stoichiometric substrate

